Research Article

Nano Research
2020, 13(6): 1558–1563

ISSN 1998-0124 CN 11-5974/O4
https://doi.org/10.1007/s12274-020-2770-4

Scalable synthesis of nanoporous silicon microparticles for highly cyclable lithium-ion batteries

Jiangyan Wang[1], William Huang[1], Yong Seok Kim[1,3], You Kyeong Jeong[1], Sang Cheol Kim[1], Jeffrey Heo[1], Hiang Kwee Lee[1], Bofei Liu[1], Jaehou Nah[3], and Yi Cui[1,2] (✉)

[1] *Department of Materials Science and Engineering, Stanford University, Stanford, California 94305, USA*
[2] *Stanford Institute for Materials and Energy Sciences, SLAC National Accelerator Laboratory, 2575 Sand Hill Road, Menlo Park, California 94025, USA*
[3] *R&D center, Samsung SDI, 130, Samsung-ro, Yeongtong-gu, Suwon-si, Gyeonggi-do 16678, Republic of Korea*

Received: 27 January 2020 / **Revised:** 20 March 2020 / **Accepted:** 21 March 2020

ABSTRACT

Nanoporous silicon is a promising anode material for high energy density batteries due to its high cycling stability and high tap density compared to other nanostructured anode materials. However, the high cost of synthesis and low yield of nanoporous silicon limit its practical application. Here, we develop a scalable, low-cost top-down process of controlled oxidation of Mg_2Si in the air, followed by HCl removal of MgO to generate nanoporous silicon without the use of HF. By controlling the synthesis conditions, the oxygen content, grain size and yield of the porous silicon are simultaneously optimized from commercial standpoints. *In situ* environmental transmission electron microscopy reveals the reaction mechanism; the Mg_2Si microparticle reacts with O_2 to form MgO and Si, while preventing SiO_2 formation. Owing to the low oxygen content and microscale secondary structure, the nanoporous silicon delivers a higher initial reversible capacity and initial Coulombic efficiency compared to commercial Si nanoparticles (3,033 mAh/g vs. 2,418 mAh/g, 84.3% vs. 73.1%). Synthesis is highly scalable, and a yield of 90.4% is achieved for the porous Si nanostructure with the capability to make an excess of 10 g per batch. Our synthetic nanoporous silicon is promising for practical applications in next generation lithium-ion batteries.

KEYWORDS

silicon anode, nanoporous microparticle, yield, lithium-ion battery, Coulombic efficiency

1 Introduction

The implementation of next generation lithium-ion batteries (LIBs) is predicated on the availability of low-cost, energy-dense electrode materials [1–5]. A variety of emerging anode and cathode materials have attracted intensive attention [6–11]. Among them, silicon (Si) stands out as a promising anode material for next generation LIBs due to its high theoretical specific capacity (4,200 mAh/g, $Li_{22}Si_5$), which is more than ten times the theoretical capacity of conventional graphite anodes [12, 13]. Successful implementation of a silicon anode will enable advanced lithium-ion battery chemistries and help reduce the cell cost.

Despite its high capacity, Si suffers from poor cycling stability caused by its large volume change (> 300%) during lithiation/delithiation processes, resulting in electrode pulverization and continued growth of the solid-electrolyte interphase (SEI) which has been widely analyzed through cryogenic electron microscopy [14–20]. Generally, reducing the size of silicon to the nanoscale in at least one dimension can alleviate the stress and can even prevent fracture. Various Si nanostructures including nanoparticles, nanorods, nanowires, nanotubes, nanosheets, etc. have demonstrated an improved cycling life compared to their bulk counterparts [21–29]. However, these Si nanostructures suffer from low initial Coulombic efficiency (ICE) due to their large specific surface area, resulting in significant SEI growth, along with low volumetric energy density due to their low tap density [30]. Microscale porous Si particles assembled from nanostructured subunits could deliver a higher ICE and volumetric energy density while simultaneously retain good cycling stability with preserved void space to buffer the volume expansion. Although many guidelines for designing these high-performance porous silicon anodes have been established, synthetic methods are still limited to high temperature or high energy processes and mostly involve the use of corrosive hydrofluoric acid (HF) [31, 32]. In addition, the yield of the Si product remains low [33–36]. Moreover, the correlation between the synthesis condition and the properties of Si product is a key point but often inadequately explored [37, 38]. It is highly desirable yet challenging to develop safe, low-cost, and scalable fabrication methods to produce microscale porous Si anodes with high yield and good electrochemical performance.

Here, we synthesize nanoporous silicon microparticles through a scalable fluoride-free demagnesiation process of low-cost Mg_2Si. *In situ* environmental transmission electron microscopy (ETEM) reveals that Mg_2Si reacting with O_2 can be controlled to form MgO and Si, with little SiO_x detected. By controlling the synthesis condition, the oxygen content, grain size and yield of the porous silicon nanostructure are simultaneously optimized to satisfy commercial requirements.

Address correspondence to yicui@stanford.edu

The oxygen content of our synthesized porous Si is only 8%, which is lower than 12% of commercial Si nanoparticles, leading to lower irreversible lithium loss to the lithiation of the native silicon oxide. The micro-sized three-dimensional (3D) structure consists of interconnected nanograins which provide good electrical conductivity and decrease SEI formation by inhibiting electrolyte from entering the particle core. As a result, the porous silicon nanostructure delivers a high reversible capacity of 3,033 mAh/g, which is much higher than 2,418 mAh/g of the commercial silicon nanoparticle. In addition, both a high initial Coulombic efficiency of 84.3% (73.1% for commercial silicon nanoparticle) and high later-cycle Coulombic efficiencies of 99.5%–99.9% are achieved. The yield of the porous Si product is as high as 90.4% with a production capacity of 10 g/batch in the lab, which indicates the high scalability of this process. The high performance and scalability of our synthesized 3D nanoporous silicon microparticle are highly promising for practical application in high-energy lithium-ion batteries.

2 Results and discussion

2.1 Synthesis and characterization of porous Si microparticle

The synthesis process of porous Si is shown in Fig. 1(a). Commercially available Mg_2Si particles (3–12 mm) were first ball-ball milled to decrease the size to 1–15 μm (Fig. 1(c) and Table S1 in the Electronic Supplementary Material (ESM)). These Mg_2Si particles were then annealed under air atmosphere. During the annealing process, Mg_2Si reacts with O_2 to produce MgO while Si is separated forming MgO/Si composite ($Mg_2Si + O_2 \rightarrow 2MgO + Si$). The MgO was removed in diluted hydrochloric acid (HCl) aqueous solution, leaving a 3D porous silicon nanostructure consisting of crystalline Si nanoparticle subunits and nanopores. Scanning electron microscopy (SEM) images of the products obtained at different steps in the synthesis process are shown in Fig. 1(c). The surface morphology and structure change dramatically. The surface of Mg_2Si particle before annealing is smooth and intact, which becomes rough and granular after annealing. After etching away MgO, a highly porous surface is clearly observed for the final porous Si product. Additionally, the size of porous Si nanostructure is slightly larger than that of Mg_2Si precursor (Table S1 in the ESM), which is reasonable considering that the insertion of oxygen into the Mg_2Si particle during annealing could enlarge the particle size. X-ray diffraction (XRD) pattern (Fig. 1(d)) shows that the produced porous Si is crystalline and highly purified without any impurity peaks observed. X-ray photoelectron spectroscopy (XPS) shows the coexistence of Si and SiO_2 which could be due to the natural oxidation of the Si surface (Fig. 1(e)).

Considering that the oxidation behavior of both Mg and Si could be significantly affected by the annealing temperature, a series of related experiments concerning the heating of Mg_2Si in air were carried out at 400, 550 and 600 °C (Fig. S1 in the ESM). After Mg_2Si was heated to 400 °C, un-reacted Mg_2Si still can be observed even after annealing for 72 h. After annealed under 600 °C for 10 h, the Mg_2SiO_4 phase was detected in the product in addition to unreacted Mg_2Si as well as MgO and Si phases. Mg_2SiO_4 is the product of the reaction of MgO with SiO_2 at temperatures in excess of 600 °C; it cannot be removed by HCl etching and thus must be avoided in the products [39, 40]. Comparatively, after Mg_2Si was heated to 550 °C and held for 20 h, no Mg_2SiO_4 phase was detected in the product with comparatively low ratio of unreacted Mg_2Si to that annealed under 400 °C for 72 h. Since the oxidization of Mg_2Si can easily

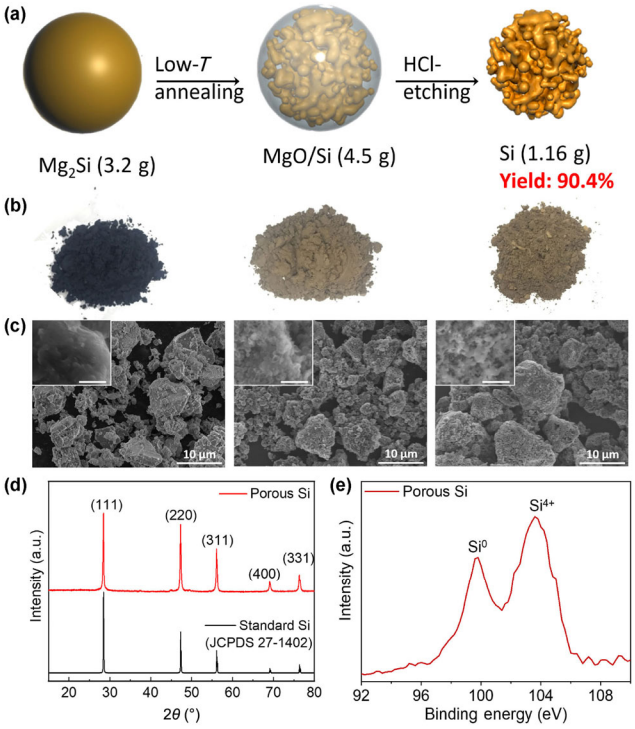

Figure 1 The synthesis of porous Si microparticles. (a) Schematic showing the synthesis process of porous Si microparticles (*T* means temperature). (b) Optical images and (c) SEM images of the products obtained during different synthesis steps. From left to right: Mg_2Si, MgO/Si and porous Si microparticles. The scale bar for the inserted high-magnification SEM is 300 nm. (d) XRD pattern and (e) XPS spectrum of as-synthesized porous Si nanostructure.

proceed by increasing the annealing duration, 550 °C was chosen as the optimal annealing temperature for the synthesis of porous silicon.

In addition to annealing temperature, annealing duration is another key parameter which determines the morphology, structure, oxygen content, grain size and yield of the porous Si products. Figure 2(a) shows the XRD pattern of the products obtained at 550 °C for 5–30 h annealing duration. The intensity of peaks corresponding to Mg_2Si decreases as the annealing duration increases, indicating that more Mg_2Si reacts with O_2 as annealing proceeds. During the removal of MgO through HCl-etching treatment, the unreacted Mg_2Si also reacts with HCl, becoming $MgCl_2$ and SiH_4 gas which runs away. Consequently, shorter annealing results in a lower yield of silicon product. Nevertheless, a high yield of porous silicon product of 90.4% and 91%, is delivered after annealing for 20 and 30 h, respectively (Fig. 2(b)), indicating that the yield of our porous silicon nanostructure is promising for commercial application. In addition, the oxygen content of the porous silicon nanostructure increases as the annealing duration increases (Fig. 2(b)), which is ascribed to the slow oxidation of Si nanograins during annealing under air atmosphere. Regardless, an oxygen content of 8% and 10.5% was achieved after annealed for 20 and 30 h, respectively, both of which are lower than that of the commercial Si nanoparticle of 12%. Moreover, although highly porous structures are always obtained after different annealing durations (Figs. 2(c)–2(e)), the size of nanograins embedded in the porous silicon nanostructure increases as annealing duration increases (Figs. 2(f)–2(h) and Figs. S2 and S3 in the ESM). The grain sizes are approximately 50 and 60 nm after annealing for 20 and 30 h, respectively. Both the oxygen content and grain size could greatly affect the initial Coulombic efficiency. The ICE increases as the oxygen content

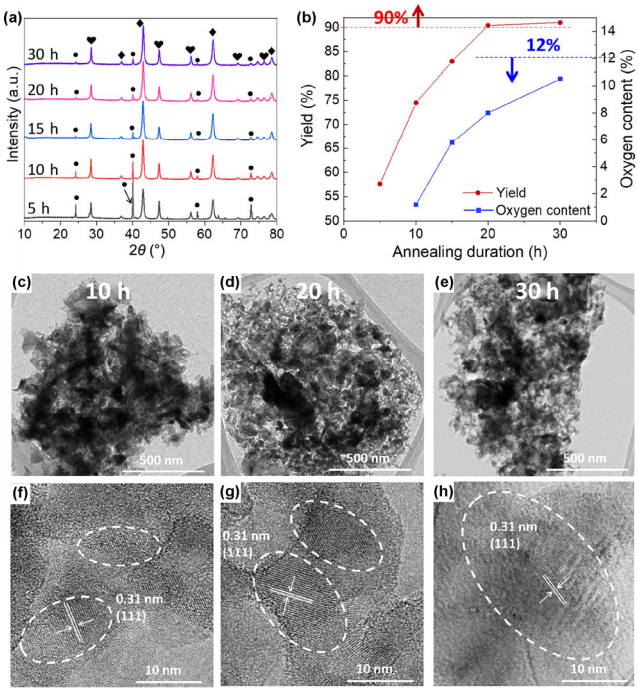

Figure 2 Effect of annealing duration on the products. (a) XRD patterns of products obtained by annealing Mg_2Si at 550 °C for 5–30 h. (● Mg_2Si (35-0773); ♥ Si (27-1402); ◆ MgO (45-0946). (b) The correlation between the annealing duration and the Si yield as well as the oxygen content of porous Si. (c)–(e) TEM and (f)–(h) HRTEM of porous Si obtained after annealing for different durations, (c) and (f) 10 h, (d) and (g) 20 h and (e) and (h) 30 h.

decreases since the silicon oxide can irreversibly trap lithium [27]; the ICE also decreases along with the decrease of grain size since the smaller grain size provides a larger surface area for SEI formation.

2.2 *In situ* environmental TEM study on the oxidation process of Mg_2Si

To fully explore the composition and structure evolution of Mg_2Si particle during the annealing process, *in situ* ETEM characterization was carried out on the oxidation reaction process at 550 °C under oxygen atmosphere. To monitor the reaction between Mg_2Si and O_2 gas in real time, dry (99.999 vol.% purity) O_2 is introduced inside the environmental TEM with the sample at 550 °C. Structural analysis by high-resolution TEM (HRTEM) and selected area electron diffraction (SAED) helps to identify the annealing products (Movies ESM1 and ESM2 and Fig. 3). A uniform single crystal Mg_2Si particle was observed before reaction, which becomes polycrystalline as new phases emerge during annealing. TEM reveals the emergence of new crystalline orientations, beginning at the edge of the particle and progressing into the particle. New phases of MgO and Si are clearly detected through SAED while the interior Mg_2Si remained unreacted (Figs. 3(c) and 3(d))). This suggests a diffusion-limited reaction; following a rapid surface reaction, the oxygen must diffuse through the MgO and Si product to further react with the interior Mg_2Si. After annealing for 40 min, the particle becomes even more nonuniform due to more MgO and Si nanograins formed as annealing duration increases. The SAED reflections corresponding to Mg_2Si reactant become weaker while those corresponding to MgO and Si products become stronger, indicating more Mg_2Si is oxidized after annealing for a longer time. No crystalline silicon oxide is observed during annealing, which agrees well with the above results observed through XRD characterization.

2.3 Electrochemical performance of the porous silicon microparticle

The performance of our as-synthesized 3D porous Si microparticles was verified by electrochemical characterizations. Type 2032 coin cells were constructed by pairing porous Si electrodes with lithium foil reference/counter electrodes. Deep galvanostatic cycling tests were carried out from 0.01 to 1 V at a rate of 0.5C (1C = 4,200 mA/g), while the first activation cycle carried out from 0.005 to 1.5 V at a rate of 0.05C.

Coulombic efficiency (CE), especially the 1st cycle CE which accounts for most of the lithium ion loss and electrolyte consumption, is one of the most important parameters to evaluate the performance of a battery. As shown in Fig. 4(a) and Table 1, the initial Coulombic efficiency of porous Si microparticles obtained after annealing for 20 h reaches 84.3%, which is superior to 73.1% for the commercial Si nanoparticle and is also higher than or at least comparable to most previously-reported ICE for porous Si anodes (Table S2 in the ESM). The reasons for the higher ICE of the porous Si microparticle is ascribed to the following three aspects: First, the nanograins in the porous Si microparticle connect with each other, which decreases the specific surface area; second, the micro-sized

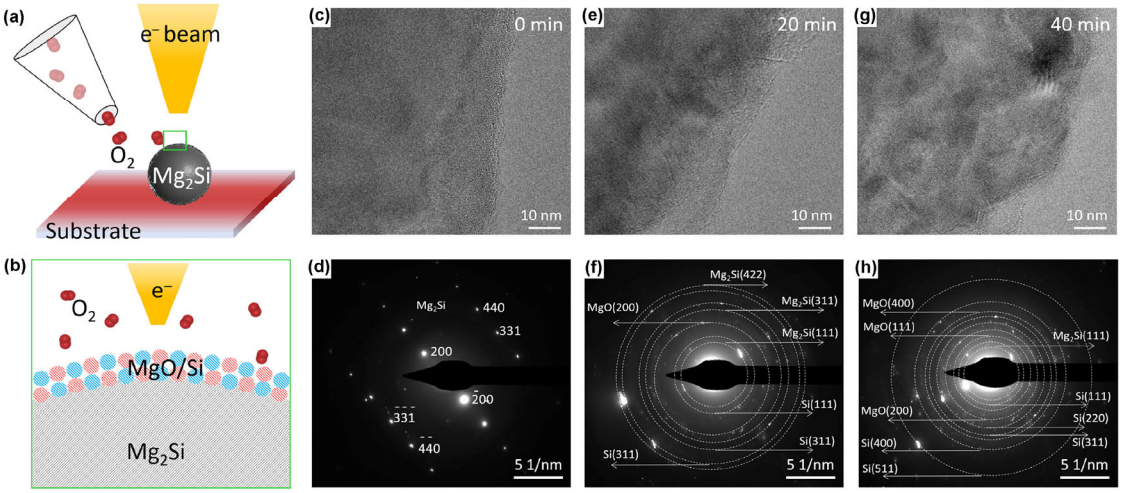

Figure 3 *In situ* ETEM characterization of the oxidation of Mg_2Si. (a) and (b) Schematic showing the oxidation process of Mg_2Si in the ETEM. (c), (e), and (g) The time-lapse images of the oxidation of Mg_2Si particle studied by ETEM (also see Movies ESM1 and ESM2), oxidation after 0 min (c), 20 min (e) and 40 min (g). (d), (f), and (h) SAED images of the observed areas in (c), (e) and (g), respectively.

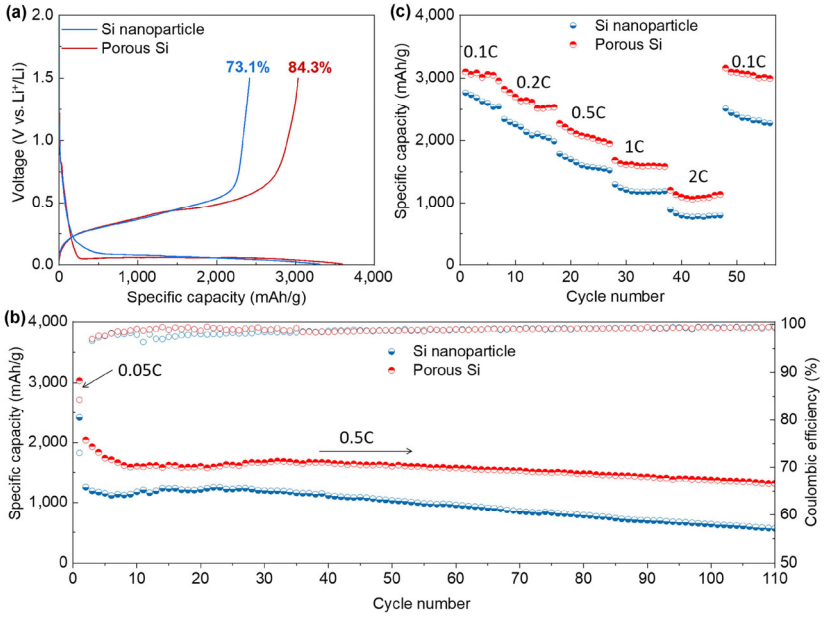

Figure 4 Electrochemical performance study. (a) First-cycle voltage profiles of individual cells with corresponding Coulombic efficiencies. (b) Cycling stability and (c) rate capability comparison of cells based on as-produced porous Si and commercial Si nanoparticle anodes.

Table 1 Effect of annealing duration on the yield, oxygen content and battery performance of porous Si products

Annealing duration	5 h	10 h	15h	20 h	30 h	Si nanoparticle
Yield (Si base, %)	57.6	74.5	83.0	90.4	91	—
Oxygen content (%)	—	1.2	5.8	8.0	10.5	12
Capacity (mAh/g)	—	3,191	—	3,033	2,995	2,418
ICE (%)	—	86.1	—	84.3	82.5	73.1

structure could inhibit the electrolyte from reaching the inner part of the micro-sized particle, thus decreasing the electrolyte–electrode contact area; third, the lower oxygen content of the porous Si induces a smaller irreversible lithium trap by the silicon oxides, which also contributes to a higher ICE. Moreover, distinct from other high-performing nano-Si anodes which require many cycles to reach Coulombic efficiency above 99% [41–43], the as-produced porous Si microparticle delivers a high Coulombic efficiency over 99% within 10 cycles and stabilizes at a high level afterwards (99.5%–99.9%).

In addition to the high initial and later-cycle Coulombic efficiencies, the porous Si also achieves a much higher reversible delithiation capacity compared to that of the commercial Si nanoparticles. The 1st cycle delithiation capacity is 3,033 and 2,418 mAh/g for porous Si microparticle and Si nanoparticle, respectively. The high reversible capacity of porous Si product indicates that the continuous nanograin subunits are electrically well connected and participate fully in the electrochemical lithiation and delithiation process. Comparatively, the relatively low capacity of commercial Si nanoparticle is due to the severe SEI formation and the weaker electrical connection since Si nanoparticles are individually separated. Moreover, the micro-sized nanoporous Si microparticle maintains a good cycling stability. As shown in Fig. 4(b), a delithiation capacity of 1,375 mAh/g is retained after 100 consecutive cycles at a high rate of 0.5C, which is over four times as large as that of the commercial graphite anodes and surpasses that of Si nanoparticles (634 mAh/g). The exceptional electrochemical stability can be attributed to the three-dimensional micro-/nanoscale architecture. The nanopores between nanograins in the microscaled particle can effectively accommodate the volume change and relieve the strain/stress upon lithiation/delithiation. The inhibited SEI formation as discussed above minimizes lithium inventory loss and electrolyte consumption, which helps to maintain a high capacity retention.

The rate capability as another important evaluation parameter is also studied using galvanostatic charge–discharge measurements by increasing the rate from 0.1C to 2C and then back to 0.1C. As shown in Fig. 4(c), even at a high rate of 2C, the electrode based on micro-sized porous Si nanostructure can still deliver a reversible capacity over 1,000 mAh/g. In addition, the capacity could recover to approximately 3,000 mAh/g when the current rate is decreased back to 0.1C. The superior rate capability is benefited from the good electrical conductivity provided by the interconnected nanograins, short Li^+ ion diffusion offered by the nano-sized grains, and decreased side reactions with the electrolyte.

3 Conclusion

In summary, we develop three-dimensional nanoporous silicon microparticles with high yield and high Coulombic efficiency through a scalable low-cost fluoride-free approach. *In situ* environmental TEM reveals the oxidation process of Mg_2Si precursor, with only MgO and Si formed. By controlling the synthesis condition, the oxygen content, grain size, yield and the electrochemical performance of the porous silicon nanostructure are simultaneously optimized from commercial standpoints. The low oxygen content guarantees low irreversible lithium loss to lithiation of silicon oxides. The micro-scaled three-dimensional porous architecture assembled from interconnected nanograins effectively buffering volume expansion, provides a good electrical conductivity and reduces SEI formation by limiting the access of electrolyte into the particle

core. As a result, the porous silicon nanostructure delivers a much higher initial Coulombic efficiency of 84.3% compared to 73.1% of commercial silicon nanoparticle, and a high reversible capacity of 3,033 mAh/g superior to 2,418 mAh/g of the silicon nanoparticle. In addition, the porous silicon nanostructure also achieves a good cycling stability and rate capability. Moreover, the yield of the porous Si product is as high as 90.4%. This work sheds light on the rational design of Si anodes for practical high-energy lithium-ion batteries.

Acknowledgements

This work was supported by Samsung SDI. Part of this work was performed at the Stanford Nano Shared Facilities (SNSF) and Stanford Nanofabrication Facility (SNF).

Electronic Supplementary Material: Supplementary material (XRD patterns, TEM and HRTEM images, and *in situ* videos) is available in the online version of this article at https://doi.org/10.1007/s12274-020-2770-4.

References

[1] Aricò, A. S.; Bruce, P.; Scrosati, B.; Tarascon, J. M.; van Schalkwijk, W. Nanostructured materials for advanced energy conversion and storage devices. *Nat. Mater.* **2005**, *4*, 366–377.

[2] Armand, M.; Tarascon, J. M. Building better batteries. *Nature* **2008**, *451*, 652–657.

[3] Liu, Y. Y.; Zhou, G. M.; Liu, K.; Cui. Y. Design of complex nanomaterials for energy storage: Past success and future opportunity. *Acc. Chem. Res.* **2017**, *50*, 2895–2905.

[4] Sun, Y. M.; Liu, N.; Cui. Y. Promises and challenges of nanomaterials for lithium-based rechargeable batteries. *Nat. Energy* **2016**, *1*, 16071.

[5] Pomerantseva, E.; Bonaccorso, F.; Feng, X. L.; Cui, Y.; Gogotsi, Y. Energy storage: The future enabled by nanomaterials. *Science* **2019**, *366*, eaan8285.

[6] Chan, C. K.; Peng, H. L.; McIlwrath, K.; Zhang, X. F.; Huggins, R. A.; Cui, Y. High-performance lithium battery anodes using silicon nanowires. *Nat. Nanotechnol.* **2008**, *3*, 31–35.

[7] Yang, S. F.; Zavalij, P. Y.; Whittingham. M. S. Anodes for lithium batteries: Tin revisited. *Electrochem. Commun.* **2003**, *5*, 587590.

[8] Zheng, G. Y.; Lee, S. W.; Liang, Z.; Lee, H. W.; Yan, K.; Yao, H. B.; Wang, H. T.; Li, W. Y.; Chu, S.; Cui, Y. Interconnected hollow carbon nanospheres for stable lithium metal anodes. *Nat. Nanotechnol.* **2014**, *9*, 618–623.

[9] Bruce, P. G.; Freunberger, S. A.; Hardwick, L. J.; Tarascon, J. M. Li-O_2 and Li-S batteries with high energy storage. *Nat. Mater.* **2012**, *11*, 19–29.

[10] Dunn, B.; Kamath, H.; Tarascon, J. M. Electrical energy storage for the grid: A battery of choices. *Science* **2011**, *334*, 928–935.

[11] Wang, J. Y.; Tang, H. J.; Zhang, L. J.; Ren, H.; Yu, R. B.; Jin, Q.; Qi, J.; Mao, D.; Yang, M.; Wang, Y. et al. Multi-shelled metal oxides prepared via an anion-adsorption mechanism for lithium-ion batteries. *Nat. Energy* **2016**, *1*, 15050.

[12] Wu, H.; Cui. Y. Designing nanostructured Si anodes for high energy lithium ion batteries. *Nano Today* **2012**, *7*, 414–429.

[13] Wang, J. Y.; Cui, Y.; Wang. D. Design of hollow nanostructures for energy storage, conversion and production. *Adv. Mater.* **2019**, *31*, 1801993.

[14] Li, Y. Z.; Yan, K.; Lee, H. W.; Lu, Z. D.; Liu, N.; Cui, Y. Growth of conformal graphene cages on micrometre-sized silicon particles as stable battery anodes. *Nat. Energy* **2016**, *1*, 15029.

[15] Wang, J. Y.; Liao, L.; Li, Y. Z.; Zhao, J.; Shi, F. F.; Yan, K.; Pei, A.; Chen, G. X.; Li, G. D.; Lu, Z. Y. et al. Shell-protective secondary silicon nanostructures as pressure-resistant high-volumetric-capacity anodes for lithium-ion batteries. *Nano Lett.* **2018**, *18*, 7060−7065.

[16] Wang, J. Y.; Liao, L.; Lee, H. R.; Shi, F. F.; Huang, W.; Zhao, J.; Pei, A.; Tang, J.; Zheng, X. L.; Chen, W. et al. Surface-engineered mesoporous silicon microparticles as high-Coulombic-efficiency anodes for lithium-ion batteries. *Nano Energy* **2019**, *61*, 404–410.

[17] Huang, W.; Wang, J.; Braun, M. R.; Zhang, Z.; Li, Y.; Boyle, D. T.; Mclntyre, P. C.; Cui, Y. Dynamic structure and chemistry of the silicon solid-electrolyte interphase visualized by cryogenic electron microscopy. *Matter* **2019**, *1*, 1232–1245.

[18] Li, Y. Z.; Huang, W.; Li, Y. B.; Pei, A.; Boyle, D. T.; Cui, Y. Correlating structure and function of battery interphases at atomic resolution using Cryoelectron microscopy. *Joule* **2018**, *2*, 2167–2177.

[19] Huang, W.; Boyle, D. T.; Li, Y. Z.; Li, Y. B.; Pei, A.; Chen, H.; Cui, Y. Nanostructural and electrochemical evolution of the solid-electrolyte interphase on CuO nanowires revealed by cryogenic-electron microscopy and impedance spectroscopy. *ACS Nano* **2019**, *13*, 737–744.

[20] Li, Y. Z.; Li, Y. B.; Cui, Y. Catalyst: How Cryo-EM shapes the development of next-generation batteries. *Chem* **2018**, *4*, 2250–2256.

[21] Liu, N.; Wu, H.; McDowell, M. T.; Yao, Y.; Wang, C. M.; Cui, Y. A yolk-shell design for stabilized and scalable Li-ion battery alloy anodes. *Nano Lett.* **2012**, *12*, 3315−3321.

[22] Zhou, Y. L.; Jiang, X. L.; Chen, L.; Yue, J.; Xu, H. Y.; Yang, J.; Qian, Y. T. Novel mesoporous silicon nanorod as an anode material for lithium ion batteries. *Electrochim. Acta* **2014**, *127*, 252–258.

[23] Soleimani-Amiri, S.; Tali, S. A. S.; Azimi, S.; Sanaee, Z.; Mohajerzadeh, S. Highly featured amorphous silicon nanorod arrays for high-performance lithium-ion batteries. *Appl. Phys. Lett.* **2014**, *105*, 193903.

[24] Cui, L. F.; Ruo, R.; Chan, C. K.; Peng, H. L.; Cui, Y. Crystalline-amorphous core-shell silicon nanowires for high capacity and high current battery electrodes. *Nano Lett.* **2009**, *9*, 491–495.

[25] Xiao, Y.; Hao, D.; Chen, H. X.; Gong, Z. L.; Yang, Y. Economical synthesis and promotion of the electrochemical performance of silicon nanowires as anode material in Li-ion batteries. *ACS Appl. Mater. Interfaces* **2013**, *5*, 1681–1687.

[26] Park, M. H.; Kim, M. G.; Joo, J.; Kim, K.; Kim, J.; Ahn, S.; Cui, Y.; Choi, J. Silicon nanotube battery anodes. *Nano Lett.* **2009**, *9*, 3844–3847.

[27] Wu, H.; Chan, G.; Choi, J. W.; Ryu, I.; Yao, Y.; McDowell, M. T.; Lee, S. W.; Jackson, A.; Yang, Y.; Hu, L. B. et al. Stable cycling of double-walled Si nanotube battery anodes through solid-electrolyte interphase control. *Nat. Nanotechnol.* **2012**, *7*, 310–315.

[28] Ryu, J.; Hong, D.; Choi, S.; Park, S. Synthesis of ultrathin Si nanosheets from natural clays for lithium-ion battery anodes. *ACS Nano* **2016**, *10*, 2843−2851.

[29] Kim, W. S.; Hwa, Y.; Shin, J. H.; Yang, M.; Sohn, H. J.; Hong, S. H. Scalable synthesis of silicon nanosheets from sand as an anode for Li-ion batteries. *Nanoscale* **2014**, *6*, 4297–4302.

[30] Liu, N.; Lu, Z. D.; Zhao, J.; McDowell, M. T.; Lee, H. W.; Zhao, W. T.; Cui, Y. A pomegranate-inspired nanoscale design for large-volume-change lithium battery anodes. *Nat. Nanotechnol.* **2014**, *9*, 187–192.

[31] Yi, R.; Dai, F.; Gordin, M. L.; Chen, S. R.; Wang, D. H. Micro-sized Si-C composite with interconnected nanoscale building blocks as high-performance anodes for practical application in lithium-ion batteries. *Adv. Energy Mater.* **2013**, *3*, 295–300.

[32] Kim, H.; Han, B.; Choo, J.; Cho. J. Three-dimensional porous silicon particles for use in high-performance lithium secondary batteries. *Angew. Chem., Int. Ed.* **2008**, *47*, 10151.

[33] Ren, W. F.; Wang, Y. H.; Zhang, Z. L.; Tan, Q. Q.; Zhong, Z. Y.; Su, F. B. Carbon-coated porous silicon composites as high performance Li-ion battery anode materials: Can the production process be cheaper and greener. *J. Mater. Chem. A* **2016**, *4*, 552–560.

[34] Liu, N.; Huo, K. F.; McDowell, M. T.; Zhao, J.; Cui. Y. Rice husks as a sustainable source of nanostructured silicon for high performance Li-ion battery anodes. *Sci. Rep.* **2013**, *3*, 1919.

[35] Liang, J. W.; Wei, D. H.; Lin, N.; Zhu, Y. C.; Li, X. N.; Zhang, J. J.; Fan, L.; Qian, Y. T. Low temperature chemical reduction of fusional sodium metasilicate nonahydrate into a honeycomb porous silicon nanostructure. *Chem. Commun.* **2014**, *50*, 6856–6859.

[36] Ge, M. Y.; Lu, Y. H.; Ercius, P.; Rong, J. P.; Fang, X.; Mecklenburg, M.; Zhou, C. W. Large-scale fabrication, 3D tomography, and

lithium-ion battery application of porous silicon. *Nano Lett*. **2014**, *14*, 261−268.

[37] Liang, J. W.; Li, X. N.; Hou, Z. G.; Guo, C.; Zhu, Y. C.; Qian, Y. T. Nanoporous silicon prepared through air-oxidation demagnesiation of Mg_2Si and properties of its lithium ion batteries. *Chem*. *Commun*. **2015**, *51*, 7230−7233.

[38] Chen, M.; Li, B.; Liu, X. J.; Zhou, L.; Yao, L.; Zai, J. T.; Qian, X. F.; Yu, X. B. Boron-doped porous Si anode materials with high initial Coulombic efficiency and long cycling stability. *J. Mater*. *Chem*. *A* **2018**, *6*, 3022–3027.

[39] Chen, W.; Fan, Z. L.; Dhanabalan, A.; Chen, C. H.; Wang, C. L. Mesoporous silicon anodes prepared by Magnesiothermic reduction for lithium ion batteries. *J. Electrochem*. *Soc*. **2011**, *158*, A1055−A1059.

[40] Chun, J. Y.; An, S.; Lee, J. Highly mesoporous silicon derived from waste iron slag for high performance lithium ion battery anodes. *J. Mater*. *Chem*. *A* **2015**, 3, 21899–21906.

[41] Ruffo, R.; Hong, S. S.; Chan, C. K.; Huggins, R. A.; Cui. Y. Impedance analysis of silicon nanowire lithium ion battery anodes. *J. Phys*. *Chem*. *C* **2009**, *113*, 11390−11398.

[42] Gauthier, M.; Mazouzi, D.; Reyter, D.; Lestriez, B.; Moreau, P.; Guyomard, D.; Roue, L. A low-cost and high performance ball-milled Si-based negative electrode for high-energy Li-ion batteries. *Energy Environ*. *Sci*. **2013**, *6*, 2145−2155.

[43] Lin, D. C.; Lu, Z. D.; Hsu, P. C.; Lee, H. R.; Liu, N.; Zhao, J.; Wang, H. T.; Liu, C.; Cui, Y. A high tap density secondary silicon particle anode fabricated by scalable mechanical pressing for lithium-ion batteries. *Energy Environ*. *Sci*. **2015**, *8*, 2371−2376.

Table of contents

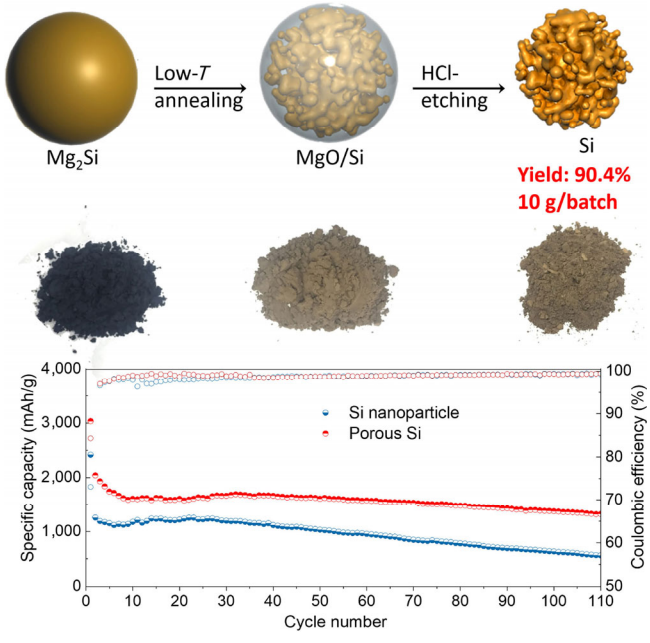

Nanoporous silicon microparticles with a high yield and production capacity were developed through a scalable, low-cost and HF-free approach. As anode materials for lithium-ion batteries, the nanoporous silicon delivered a much higher reversible capacity and Coulombic efficiency than commercial silicon nanoparticles.

Electronic Supplementary Material

Scalable synthesis of nanoporous silicon microparticles for highly cyclable lithium-ion batteries

Jiangyan Wang[1], William Huang[1], Yong Seok Kim[1,3], You Kyeong Jeong[1], Sang Cheol Kim[1], Jeffrey Heo[1], Hiang Kwee Lee[1], Bofei Liu[1], Jaehou Nah[3], and Yi Cui[1,2] (✉)

[1] *Department of Materials Science and Engineering, Stanford University, Stanford, California 94305, USA*
[2] *Stanford Institute for Materials and Energy Sciences, SLAC National Accelerator Laboratory, 2575 Sand Hill Road, Menlo Park, California 94025, USA*
[3] *R&D center, Samsung SDI, 130, Samsung-ro, Yeongtong-gu, Suwon-si, Gyeonggi-do 16678, Republic of Korea*

Supporting information to https://doi.org/10.1007/s12274-020-2770-4

File includes:

1. Materials and methods;
2. Figures S1 to S3.
3. Tables S1 and S2.
4. Supplementary references.
5. Caption for Movies ESM1 and ESM2.

Materials and methods

Synthesis of nanoporous silicon microparticles. Commercially available Mg_2Si particles (3-12 mm, Alfa Aesar) was ball milled under Argon gas at a speed of 400 rpm for 4h. In a typical thermal annealing process, ball-milled Mg_2Si particles were heated to 400-600 °C with a heating rate of 5 °C/min and kept for a certain time under air atmosphere. To remove the MgO matrix, the annealed samples were taken out of the tube at temperatures below 50 °C and immersed in 0.1-1 M hydrochloric acid aqueous solution at room temperature for 2 h. The obtained porous Si microparticles were collected by filtration and washed with distilled water and ethanol in sequence several times. The final product was dried in a vacuum oven at 60 °C for 2 h and stored in a glovebox for further use.

Materials characterization. Characterizations were carried out using scanning electron microscopy (FEI Sirion, Nova NanoSEM), transmission electron microscopy (FEI Tecnai, Titan), X-ray Diffraction (PANalyticalX'Pert, Ni-filtered Cu Kα radiation), X-ray photoelectron spectroscopy (SSI S-Probe Monochromatized, Al Kα radiation at 1486 eV) and electrochemical impedance spectroscopy (BioLogic VMP3).

In situ environmental TEM characterization. The environmental transmission electron microscope (ETEM) experiments were carried out using a FEI Titan 80-300 ETEM operated at 300 kV. The microscope was equipped with an aberration corrector in the image forming (objective lens) and a Gatan 966 Quantum electron energy loss (EEL) spectrometer. After heating up to 550 °C, we introduced oxygen gas into the ETEM and observed the reaction with Mg2Si in real time. The pressure in the microscope chamber was monitored using an Edwards Barocell 600 capacitance manometer, with a precision of ±3%. After the oxidation reaction was complete, the temperature is cooled down to room temperature and oxygen gas was pumped out of the ETEM, and HRTEM and SAED images of the particles were collected.

Electrochemistry characterization. Working electrodes were all prepared using a conventional slurry method. Porous silicon microparticle or commercial silicon nanoparticle active material, carbon black conductive additive (Super P, TIMCAL, Switzerland), and polyvinylidene fluoride (PVDF, Kynar HSV 900) binder with a mass ratio of 8:1:1 were dispersed in N-methyl-2-pyrrolidone (NMP) and stirred for 12 h. After casting onto a 15 μm-thick Cu foil and drying at 60 °C in a vacuum oven for 12 h, the samples were calendered and cut into 1 cm^2 circular disks with a mass loading of around 1 mg cm-2. In an Ar-filled glovebox, these working electrodes were assembled into type 2032 coin cells with a polymer separator (Celgard 2250) and Li metal (Alfa Aesar) as the counter/reference electrode. 100 μl of 1.0 M LiPF6 in 89 vol% 1:1 w/w ethylene carbonate/diethyl carbonate (BASF Selectilyte LP40) with 10 vol% fluoroethylene carbonate and 1 vol% vinylene carbonate (Novolyte Technologies) was added as the electrolyte with full wetting of both working and counter electrode surfaces. Coin cells were loaded into a battery test (Land Instruments) and cycled between 0.01 and 1 V at a rate of 0.5C (0.005 to 1.5 V at a rate of 0.05C for the first activation cycle). For rate capability test, coin cells were cycled at a rate of 0.1C to 2C, and then back to 0.1C. Charge/discharge rates were calculated assuming Si's theoretical capacity (4,200 mAh g^{-1} Si). Coulombic efficiency was calculated using the ratio of delithiation ($C_{dealloy}$) capacity to lithiation (C_{alloy}) capacity ($C_{dealloy}/C_{alloy} \times 100\%$).

Address correspondence to yicui@stanford.edu

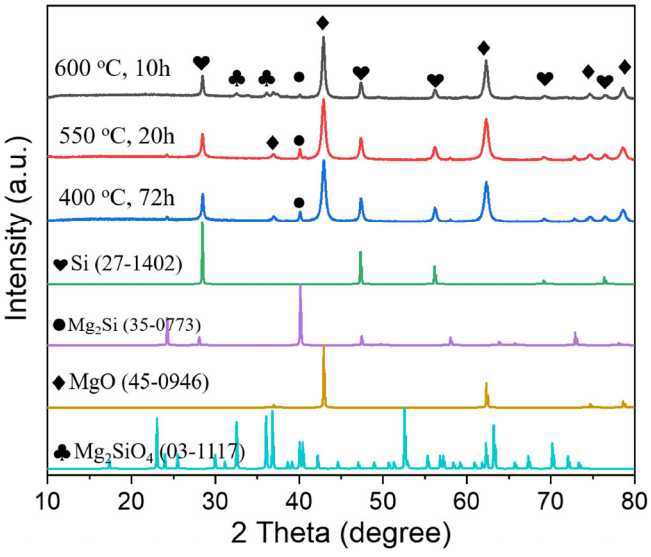

Figure S1 Effect of the annealing temperature on the compositions of products. Standard Si (27-1402) represented by ♥; Standard Mg_2Si (35-0773) represented by ●; Standard MgO (45-0946) represented by ♦; Standard Mg_2SiO_4 (03-1117) represented by ♣.

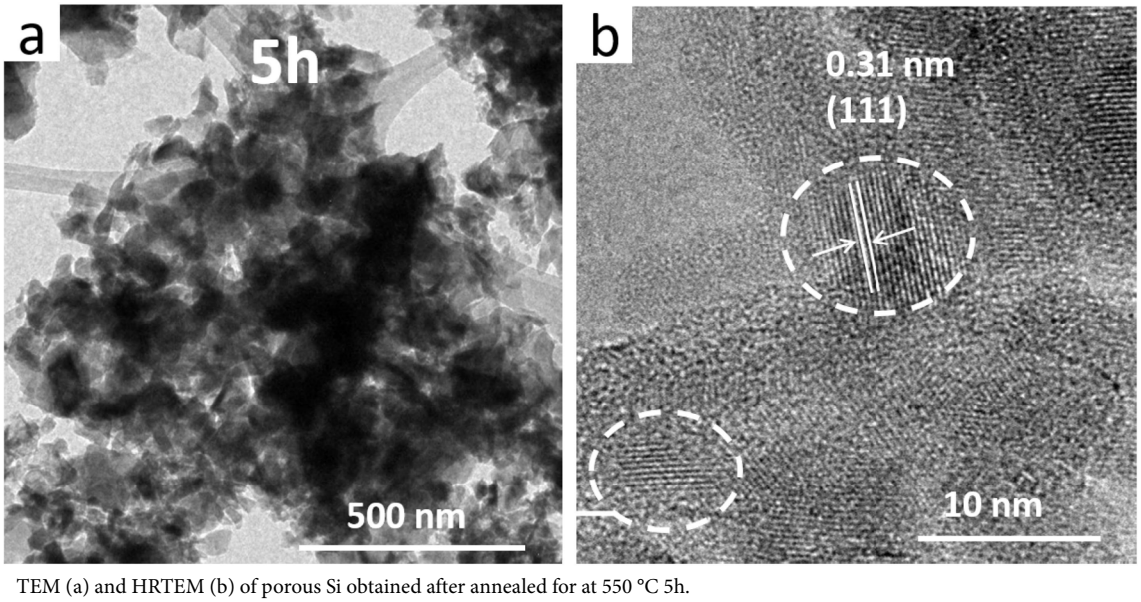

Figure S2 TEM (a) and HRTEM (b) of porous Si obtained after annealed for at 550 °C 5h.

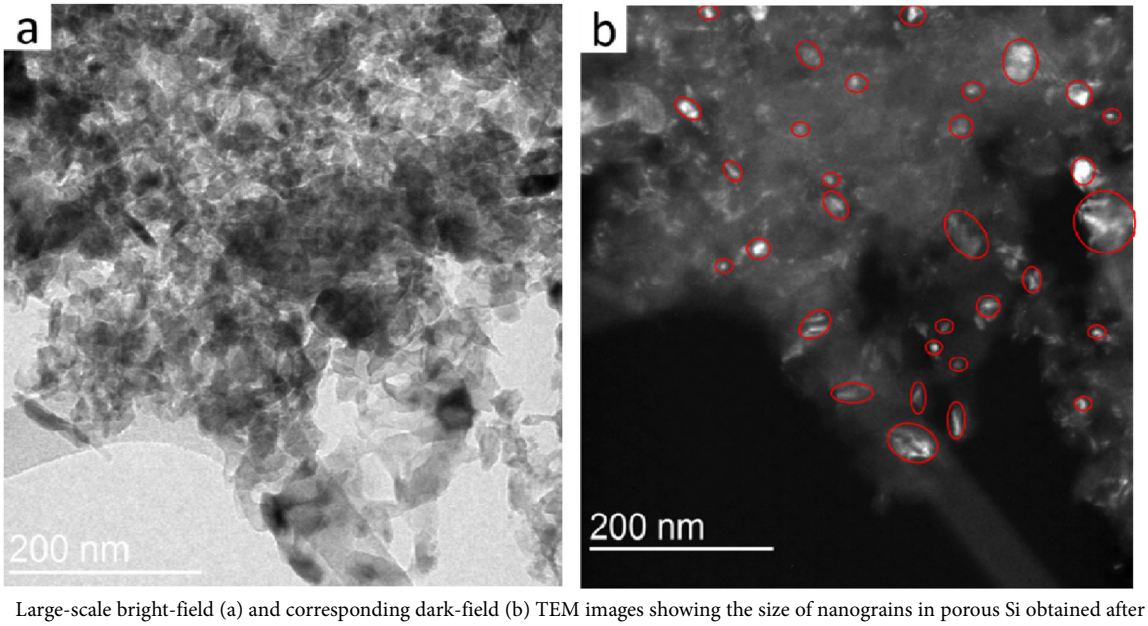

Figure S3 Large-scale bright-field (a) and corresponding dark-field (b) TEM images showing the size of nanograins in porous Si obtained after annealed for at 550 °C 20h.

Table S1 Comparison of the particle size, pore size and specific surface area of the pristine Mg2Si and porous silicon product.

	D10 (μm)	D50 (μm)	D90 (μm)	SSA (m^2/g)	Pore volume (cm^3/g)	Porosity (%)	Majority pore size (nm)
Mg_2Si	1.5	4.6	14.8	2.5	0.012	2.33	—
Porous Si	1.4	7.2	21.2	39.2	0.203	32.1	~40 (10~130)

Table S2 Comparison of the electrochemical performance of porous silicon anode materials.

Sample	Initial reversible capacity (mAh/g)	Initial Coulombic efficiency (%)	Retained capacity (mAh/g)	References
Porous Si	2416 at 0.1 A/g	73.7	1600 after 100 cycles	1
Porous Si	1700 at 0.2 A/g	62.5	952 after 300 cycles	2
Porous Si	1728 at 0.1 A/g	80.1	850 after 800	3
Porous Si	3550 at 1.8A/g	85	1000 after 300	4
Porous Si	3291 at 0.36 A/g	88	1200 after 400 cycles	5
Porous Si	2974 at 0.4 A/g	83.3	500 after 100 cycles	6
Porous Si	1256 at 0.21 A/g	37.6	560 after 10 cycles	7
Porous Si	1780 at 0.1 C	69.3	125 after 30 cycles	8
Porous Si	3033 at 0.21 A/g	84.3	1375 at 2.1 A/g after 100 cycles	This work

Supplementary references

[1] Yan, Y.; Lin, G.; Zhu, C.; Tsukimoto, S.; Aken, P. A. V.; Maier, J. Reversible storage of lithium in silver-coated three-dimensional macroporous silicon. Adv. Mater. 2010, 22, 2247-2250.

[2] Zuo, X.; Xia, Y.; Ji, Q.; Xiang, G.; Yin, S.; Wang, M.; Wang, X.; Bao, Q.; Wei, A.; Sun, Z. Self-templating construction of 3D hierarchical macro-/mesoporous silicon from 0D silica nanoparticles. ACS Nano 2017, 11, 889-899.

[3] Yoon, T.; Bok, T.; Kim, C.; Na, Y.; Park, S.; Kim, K. S. Mesoporous silicon hollow nanocubes derived from metal−organic framework template for advanced lithium-ion battery anode. ACS Nano 2017, 11, 4808–4815.

[4] Wada, T.; Ichitsubo, T.; Yubuta, K.; Segawa, H.; Yoshida, H.; Kato, H. Bulk-nanoporous-silicon negative electrode with extremely high cyclability for lithium-ion batteries prepared using a top-down process. Nano Lett. 2014, 14, 4505-4510.

[5] Liang, J.; Li, X.; Hou, Z.; Guo, C.; Zhu, Y.; Qian, Y. Nanoporous silicon prepared through air-oxidation demagnesiation of Mg2Si and properties of its lithium ion batteries. Chem. Commun. 2015, 51, 7230−7233.

[6] Chen, M.; Li, B.; Liu, X.; Zhou, L.; Yao, L.; Zai, J.; Qian, X.; Yu, X. Boron-doped porous Si anode materials with high initial coulombic efficiency and long cycling stability. J. Mater. Chem. A 2018, 6, 3022–3027.

[7] Wang, J.; Liao, L.; Lee, H. R.; Shi, F.; Huang, W.; Zhao, J.; Pei, A.; Tang, J.; Zheng, X.; Chen, W.; Cui, Y. Surface-engineered mesoporous silicon microparticles as high-Coulombic-efficiency anodes for lithium-ion batteries. Nano Energy 2019, 61, 404–410.

[8] Bang, B. M.; Lee, J. I.; Kim, H.; Cho, J.; Park, S. High-performance macroporous bulk silicon anodes synthesized by template-free chemical etching. Adv. Energy Mater. 2012, 2 878-883.

Movies

Movie ESM1 *In situ* ETEM characterization of the oxidation process of Mg_2Si annealed from 0 to 20 min.
Movie ESM2 *In situ* ETEM characterization of the oxidation process of Mg_2Si annealed from 20 to 40 min.